Catalysis Letters (2021) 151:2176–2186
https://doi.org/10.1007/s10562-020-03488-2

Synthesis and Characterization of $SrFeO_{2.73}/Bi_2MoO_6$ Heterojunction with Enhanced Photocatalytic Activity

Jifeng Guo[1,2] · Rui Liu[1,2] · Yuxuan Ma[1,2] · Meiqi Wang[1,2] · Jing Li[1,2] · Xiao Wei[1,2] · Luyao Zhao[1,2]

Received: 2 May 2020 / Accepted: 2 December 2020 / Published online: 1 January 2021

Abstract

Simple hydrothermal method and wet chemical method were both used to synthesize a novel SFO/BMO heterojunction, which was applied to the degradation of tetracycline (TC) in wastewater. Compared with the pure catalyst, the composite heterojunction catalyst can significantly improve the photodegradation efficiency. Under simulated sunlight, the degradation rate of TC by the composite with 30 wt% SFO mass could reach 77%, which was 20.8% higher than that of pure BMO and 50.4% higher than that of pure SFO. This is attributed to the low recombination rate of photogenerated electron-holes and the reduction in the band gap width caused by the synergy of BMO and SFO. At the same time, this phenomenon was confirmed by a series of characterizations, including XRD, SEM, XPS, FT-IR and UV–Vis, as well as analysis of the catalytic mechanism. The study provides a theoretical basis for the discovery of diverse photocatalysts.

Graphic Abstract

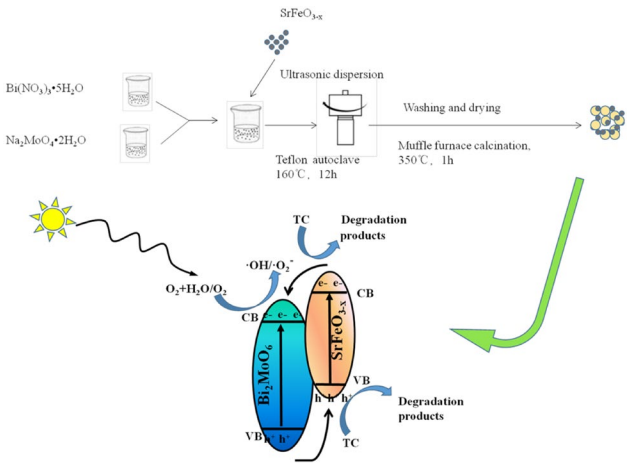

The heterojunction $Bi_2MoO_6/SrFeO_{3-x}$ is formed to reduce the recombination rate of photogenerated electron-holes, thereby improving the degradation efficiency of the original Bi_2MoO_6 to tetracycline wastewater.

Keywords $SrFeO_{2.73}/bi_2MoO_6$ heterojunction · Photocatalytic · Redox reactions · Degradation

1 Introduction

During the past few decades, water pollution has been one of the important factors contributing to environmental pollution and the global energy crisis. Among them, antibiotic wastewater, which is one of the organic wastewaters,

✉ Jifeng Guo
guojifeng@chd.edu.cn

✉ Xiao Wei
chdwx@chd.edu.cn

Extended author information available on the last page of the article

is increasingly causing serious pollution of water and soils [1]. Antibiotics mainly include tetracycline antibiotics, macrolide antibiotics, aminoglycoside antibiotics, chloramphenicol and the like. Among them, tetracycline is an important antibiotic and is widely used in human and veterinary medicine to prevent bacterial infection [2, 3]. However, due to its difficult absorption, low metabolism, abuse and overuse [4], it is easy to remain in the water and cause harm to human health. Therefore, it is necessary to develop an effective green technology to eliminate TC in the water environment.

Semiconductor photocatalysis technology is a new type of photochemical technology discovered in the 1970s [5]. Semiconductors produce photogenerated carriers—electrons (e^-) and holes (h^+) on their surface under light conditions. The reduction of electronics and the oxidization of holes can lead to the production of some active substances, such as ·OH and O_2^-. They can break down H_2O into H_2 and O_2, and can also decompose organic pollutants which are difficult to degrade in water into H_2O, CO_2 and inorganic ions. Compared with traditional water treatment method, the photocatalytic technology has the advantages of no secondary pollution, low energy consumption, simple process and high mineralization efficiency, and it is widely used in sewage treatment [4].

Many semiconductor materials, such as TiO_2, ZnO, Bi_2WO_6, CdS, etc., have been used for photocatalytic degradation of wastewater. However, these conventional photocatalysts have certain defects, such as low utilization of visible light and low quantum yield, and the n-type semiconductor Bi_2MoO_6 having the aurivillius structure can just make up for these shortcomings [6, 7]. The narrow band gap of about 2.5 eV makes it have good absorption of visible light, and its high quantum yield and non-toxicity make it continuously used in the development of new catalysts [8–11]. However, pure Bi_2MoO_6 has certain limitations on the degradation of pollutants due to the high recombination rate of electrons and holes [12]. Therefore, it needs to be modified. In addition to controlling the temperature, time and pH of the reaction to change its morphology, combining Bi_2MoO_6 with metal oxides and oxygenates to form a heterostructure is also an efficient and simple modification method. Just like the β-Bi_2O_3/Bi_2MoO_6 heterojunction of flower-like microspheres [13], $Bi_2MoO_6/BiFeO_3$ nano-heterojunction [14], etc., all of them improve the degradation efficiency of Bi_2MoO_6 on rhodamine B (RhB).

At this time, the appearance of Group IIA alkaline earth metal ferrite, such as $CaFe_2O_4$ [15, 16], $SrFe_2O_4$ [17] etc., provides a new idea for the modification of Bi_2MoO_6. Strontium ferrite is currently mainly used as a gas sensor material [18]. However, due to its unique stable spinel structure and certain magnetic properties that make it recyclable, it has also begun to be gradually used as a photocatalytic material to degrade organic wastewater, such as $SrFeO_3$ [19], $SrFeO_{3-x}$, $SrFe_{12}O_{19}$ [20] and so on. For instance, the MFe_2O_4 (M = Ca, Sr, Ba) catalyst with a band gap of about 2.0 eV prepared by Vijayaraghavan et al. has a good adsorption effect on Congo red dye [21]. Ghaffari [19] studied the effect of $SrFeO_3$ photocatalyst on the degradation efficiency of methylene blue (MB). These studies have illustrated the application prospects of strontium ferrite in photocatalysis.

Therefore, for the first time, Bi_2MoO_6 is coupled with non-stoichiometric compounds $SrFeO_{2.73}$ with a narrower band gap, which improves the degradation efficiency of Bi_2MoO_6 on antibiotic wastewater (tetracycline wastewater). In addition, the composite catalyst saves resources for improving the visible light utilization rate. Moreover, due to the magnetic properties of the $SrFeO_{2.73}$, the catalyst is easily recycled. Hence the construction of $SrFeO_{2.73}/Bi_2MoO_6$ heterojunction provides a new idea for the development of new green catalysts.

2 Experimental

2.1 Materials

Bismuth nitrate ($Bi(NO_3)_3·5H_2O$) was purchased from Tianjin Kemiou Chemical Reagent Co., Ltd. Sodium molybdate ($Na_2MoO_4·2H_2O$), ethylene glycol and anhydrous ethanol were purchased from Tianjin Damao Chemical Reagent Factory. Citric acid ($C_6H_8O_7$), strontium nitrate ($Sr(NO_3)_2$), iron nitrate ($Fe(NO_3)_3·9H_2O$) were purchased from Tianjin Tianli Chemical Reagent Co., Ltd. All chemicals were used without further purification. Tetracycline (TC) was purchased from Shanghai Yuanye Biotechnology Co., Ltd. Deionized water taken from a clear water evolution system (Manufactured in China, Merck Millipore).

2.2 Synthesis of $SrFeO_{2.73}/Bi_2MoO_6$ Heterojunction

0.25 mol/L ferric nitrate and strontium nitrate solution were prepared and used to prepare precursors. 100 mL $Fe(NO_3)_3·9H_2O$ solution and 50 mL $Sr(NO_3)_2$ solution were mixed. Next, 0.03 mol citric acid was added to the mixed solution in a 200 mL beaker to make them evenly mixed well. The mixed solution was placed in a constant temperature water bath at 70 °C, and stirred for 4 h. After that, the temperature of water bath was raised up to 80 °C, and concentrated for 5 h. Then the liquid exhibited a viscous wet gel. The wet gel was further dried at 120 °C for 8 h to obtain a bulky xerogel, and then was calcined at a high temperature of 700 °C for 2 h in a muffle furnace to obtain a $SrFeO_{2.73}$ (SFO) powder.

727.6 mg of $Bi(NO_3)_3·5H_2O$ and 181.6 mg of $Na_2MoO_4·2H_2O$ were dissolved in 7.5 mL of ethylene glycol under magnetic stirring, respectively, and then the

two solutions were mixed. Different mass ratios of SFO were ultrasonically dispersed to the solution (m (SFO): m (Bi_2MoO_6 (BMO)) = 1:9, 2:8, 3:7, 4:6, 5:5). Then 45 mL of ethanol was added into the mixture. The dispersion was transferred to a 100 mL Teflon-lined stainless steel autoclave and heated at 160 °C for 12 h, and then was cooled to room temperature. The solid product was collected and washed thoroughly with water and ethanol for 3 times, and dried in an oven at 80 °C. At last, the solid product was ground into powder and calcinated at 350 °C in a muffle furnace for 1 h (10 °C/min). Different quality percentages of SFO (10 wt%, 20 wt%, 30 wt%, 40 wt%, 50 wt%)/BMO composites were prepared, respectively. Pure BMO was prepared by the same procedure, but no SFO was added.

2.3 Characterization

Powder X-ray diffraction (XRD) was recorded using D8 Advance X-ray diffractometer analysis with Cu-Kα radiation by scanning rate of 0.04°/0.5 s from 15° to 80°. FT-IR analysis was performed using KBr particles by SPECTRUM TWO-type Fourier transform infrared spectroscopy of American PE Corporation. Elemental valence was analyzed by X-ray photo-electron spectroscopy (XPS) on a Thermo Fisher K-Alpha (USA) spectrometer. Field emission scanning electron microscopes (SEM) were performed via JSM-7800F scanning electron microscope. Transmission electron microscopy (TEM) was performed via JEOL JEM-2100 F (Japan) transmission electron microscopy. The UV–Vis diffuse reflectance spectrums of the samples were carried out on the Evolution 220 UV–Vis spectrometer of American Thermo Technology.

2.4 Photocatalytic Test

The photocatalytic properties of SFO/BMO heterojunction were measured by BL-GHX-V photochemical reaction instrument with tetracycline (TC) as the target pollutant and 300 W high-pressure xenon lamps as the simulated light source. 20 mg of photocatalysts with different compound ratios were added to a quartz tube containing 50 mL of 30 mg/L tetracycline (TC) solution, and use pure TC solution without any photocatalyst as a blank control group. The initial concentration of the solution was recorded as C_0. Firstly, the solution was magnetically stirred for 30 min under dark conditions to make the reaction reach adsorption equilibrium, and then 4 mL supernatant of suspension and centrifuge (8000 r/min, 5 min) was taken and measured at 356 nm by 752 N UV spectrophotometer to get the concentration which was record C_1. After that, the photoreaction was performed under the cooling and circulation device and the light source of the xenon lamp. In the photoreaction stage, repeat the above steps every 20 min to take a sample, and measure the absorbance record concentration C. The photocatalytic degradation efficiency of TC was calculated by the following formula.

$$\text{Photocatalytic degradation rate}(\%) = (1 - C/C_1) \times 100\% \quad (1)$$

3 Results and Discussion

3.1 XRD Analyses

The XRD pattern of the prepared sample was shown in the Fig. 1. All diffraction peaks of the pure BMO were identical to the orthorhombic Bi_2MoO_6 (JCPDS NO.72-1524). Diffraction peaks at 2θ = 23.5°, 28.3°,32.6°, 36.0°, 46.8°, 55.6°, 58.7°, 68.3° and 75.5° corresponded to the (111), (131), (002), (151), (062), (133), (262), (400), (333) planes, respectively. No other impurity peaks were observed. It could be observed that SFO showed the diffraction peaks of (111), (201), (400), (112), (510) and (402) planes at 2θ = 25.2°, 25.8°, 32.6°, 35.6°, 44.1° and 47.7°. This showed the successful synthesis of non-stoichiometric strontium iron oxide. For the SFO/BMO heterojunction, the characteristic diffraction peaks of BMO could be clearly observed. Due to the low content of SFO, the diffraction peaks of SFO were not obvious enough, except for 40 wt% and 50 wt% SFO/BMO. However, as the content of SFO increased, the diffraction peaks of BMO are gradually weakened, suggesting successful combining of the two semiconductors to produce heterojunction.

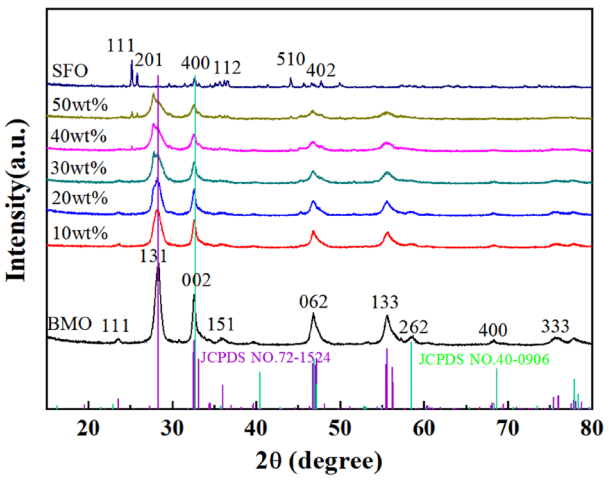

Fig. 1 XRD patterns of BMO, SFO and SFO/BMO with different composite ratios

3.2 FT-IR Analysis

The FT-IR spectra were shown in the Fig. 2. For pure phase BMO, the weak absorption band at 448 cm^{-1} could be attributed to the Bi–O bending vibration of the BiO_6 octahedron. The weak band at 566 cm^{-1} was assigned to the bending vibration of MoO_6 [22]. The asymmetric stretching mode of Mo–O could be detected at 729 cm^{-1} and 842 cm^{-1}, which was related to the vibrations of the equatorial and apical oxygen atoms in MoO_6 octahedron [23, 24]. Peaks at 1628 cm^{-1} and 3379 cm^{-1} were attributed to O–H vibration in water molecules [25]. For SFO, the absorption band at 555 cm^{-1} was caused by the stretching vibration of Sr^{2+}–O^{2-} [26]. Peaks were observed at 858 cm^{-1} and 1451 cm^{-1} corresponding to Fe–O vibration and flexural vibrations of OH groups [21].

It could be observed that all characteristic peaks of BMO were reflected in the FT-IR spectrum of the complex 30 wt% SFO/BMO. It was possible that only Sr^{2+}–O^{2-} vibration peak and O–H vibration peak could be observed due to the low content of SFO. Therefore, it could be further explained that SFO and BMO were successfully compounded together.

3.3 XPS Analysis

The surface composition of 30 wt% SFO/BMO was analyzed by X-ray photoelectron spectroscopy as shown in Fig. 3. Figure 3a showed that the composite material contained Bi, Mo, O, Sr and Fe elements. The C 1 s spectrum was mainly derived from the hydrocarbon used in the calibration of the instrument and a bit of impurity $SrCO_3$ in the heterojunction. Figure 3b showed the high resolution spectrum of Bi, the binding energies of Bi 4f 7/2 and Bi 4f 5/2 peaks in the BMO were located at 158.51 eV and 163.78 eV, respectively,

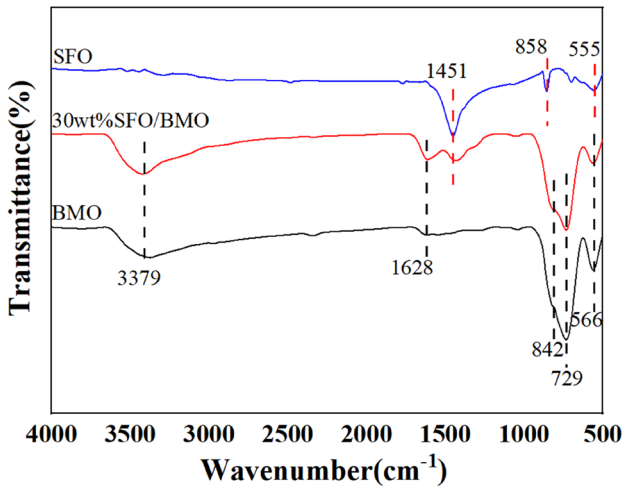

Fig. 2 FT-IR spectra of BMO, SFO and 30 wt% SFO/BMO

suggesting that Bi^{3+} existed in the samples [27]. In the Mo 3d spectra (Fig. 3c), peaks at 231.77 eV and 234.78 eV were attributed to Mo 3d 5/2 and Mo 3d 3/2 of Mo^{6+}, respectively [28]. In the O 1 s spectra (Fig. 3d),the three Gaussian peaksfitting at binding energies at 529.42 eV, 530.10 eV, 532.04 eV which are attributed to the lattice oxygen in Bi–O, lattice oxygen in Mo–O and hydroxyl groups at the surface of Bi_2MoO_6,respectively [29–31]. Figure 3e shows the high-resolution Sr 3d spectrum and the doublet peaks at 132.90 eV and 134.66 eV can be attributed to Sr $3d_{5/2}$ and Sr $3d_{3/2}$,respectively,indicating the existence of Sr^{2+} [32, 33]. XPS spectra of Fe 2p region was shown in Fig. 3f. The peaks appearing at 710.10 eV and 723.05 eV could be assigned to Fe^{4+}. The weak peak at 719.9 eV confirmed the presence of Fe^{3+} [34, 35]. This phenomenon illustrated Fe in the non-stoichiometric compound SFO coexisted as Fe^{3+} and Fe^{4+}.

3.4 SEM Analysis

The morphology and microstructure of the photocatalyst could be characterized by scanning electron microscopy (SEM). As shown in Fig. 4a, BMO basically showed an irregular spherical shape, and the particle size ranged from 1.5 to 3.5 μm. Figure 4b was a scanning image under a high-power microscope, and it could be seen that the surface was flower-shaped microspheres formed by stacking sheets. Figure 4c, d were SEM images of SFO at different scanning multiples. It could be seen that SFO was a regular sphere with a particle size of about 5 μm. Its surface was composed of filaments, similar to a velvet ball. Due to the regular spherical shape of the SFO, 30 wt% SFO/BMO heterojunction also exhibited a part of the regular spherical shape, as shown in Fig. 4e. And the spherical surface combined the characteristics of BMO and SFO. Compared with BMO, the surface area of needle-like spherical structure was greatly increased, which made the contact area between pollutants and catalyst increase, and more reaction sites could be provided for the photocatalytic degradation of TC [36]. It was beneficial to improve the photocatalytic performance.

3.5 TEM Analysis

The hierarchical structure of 30 wt% SFO/BMO was further observed and validated by transmission electron microscopy (TEM). The SFO/BMO heterojunction presented a partially regular spiculate spherical structure as shown in Fig. 5a. The high-resolution HRTEM image (Fig. 5b) showed two types of lattice fringe with lattice spacing of 0.318 nm and 0.387 nm, corresponding to the (131) crystal plane of BMO and (201) crystal plane of SFO, respectively [30, 34]. These results demonstrated that the successful preparation of SFO/BMO photocatalysts and the tight relationship between

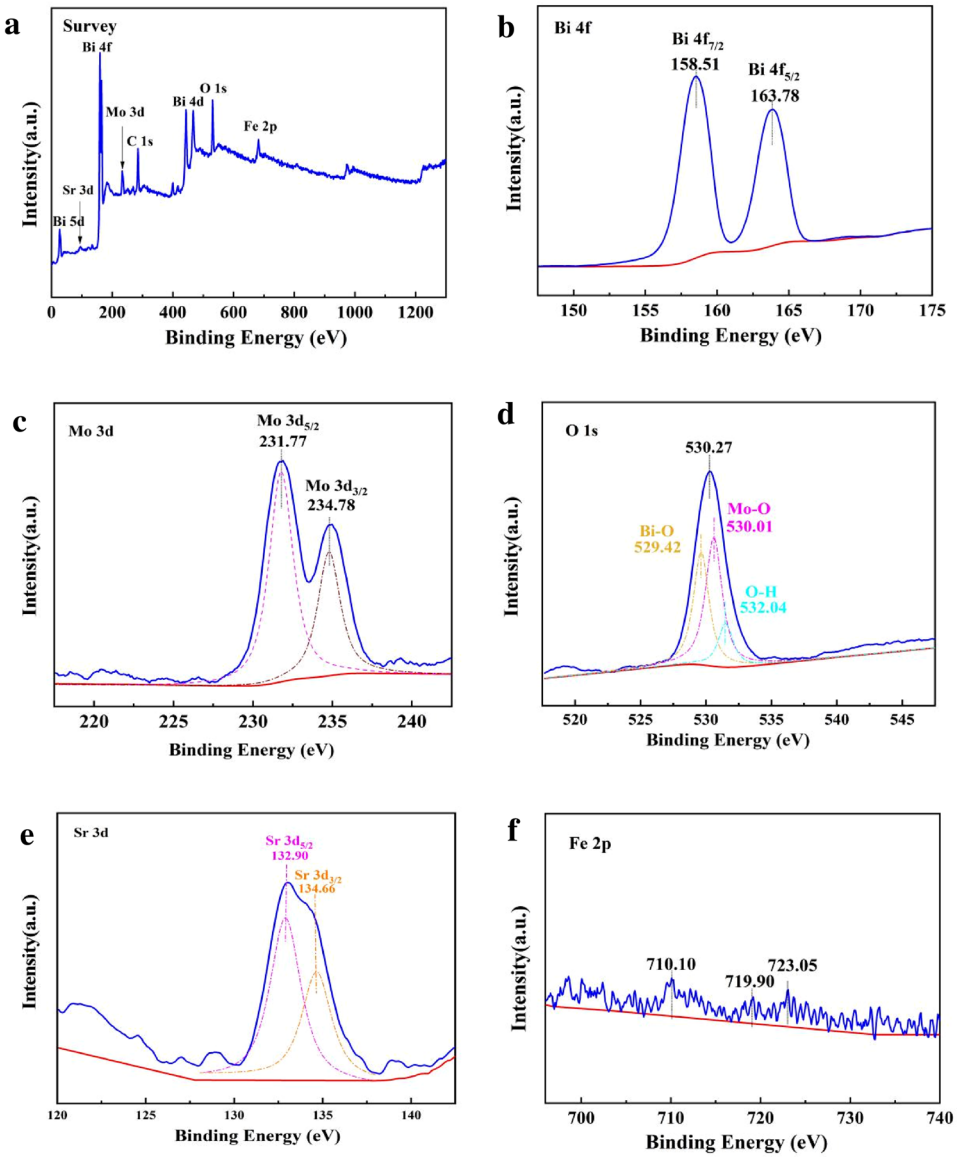

Fig. 3 **a** full spectrum of XPS spectrums of 30 wt% SFO/BMO heterojunction, **b** Bi 4f of XPS spectrums of 30 wt% SFO/BMO heterojunction, **c** Mo 3d of XPS spectrums of 30 wt% SFO/BMO heterojunction, **d** O 1 s of XPS spectrums of 30 wt% SFO/BMO heterojunction, **e** Sr 3d of XPS spectrums of 30 wt% SFO/BMO heterojunction and **f** Fe 2p of XPS spectrums of 30 wt% SFO/BMO heterojunction

BMO and SFO contribute to electron transfer in photocatalytic processes.

3.6 UV–Vis Analysis

The optical properties of SFO, BMO, and SFO/BMO were studied by UV–Vis diffuse reflectance spectra. As shown in Fig. 6a, the pure BMO exhibited a strong absorption of light from 200 to 500 nm, extending from the ultraviolet region to the visible region. Compared with BMO, SFO had strong absorption of sunlight from 200 nm, which could be extended to the infrared region, revealing its high absorption efficiency of light. For the SFO/BMO heterojunction, the absorption of ultraviolet light was enhanced compared to SFO. In addition, as the mass ratio of SFO increased, compared with BMO, the absorption of visible light also gradually increased, and its absorption sideband redshifts was from 500 nm to about 600 nm. When the mass ratio of SFO was 50 wt%, the absorption of light was the strongest. It showed that the introduction of SFO into BMO nanosheets was beneficial to the utilization of sunlight, especially visible light.

For semiconductor materials, the optical absorption follows the equation:

$$\alpha hv = K(hv - Eg)^{n/2} \quad (2)$$

where Eg, α, k, and v are the band gap, the absorption coefficient, a constant and the light frequency, respectively [37, 38]. In addition, n decides the characteristics of the transition in a semiconductor [39, 40]. For example, BMO is a direct band gap semiconductor, so n = 1, but SFO is an

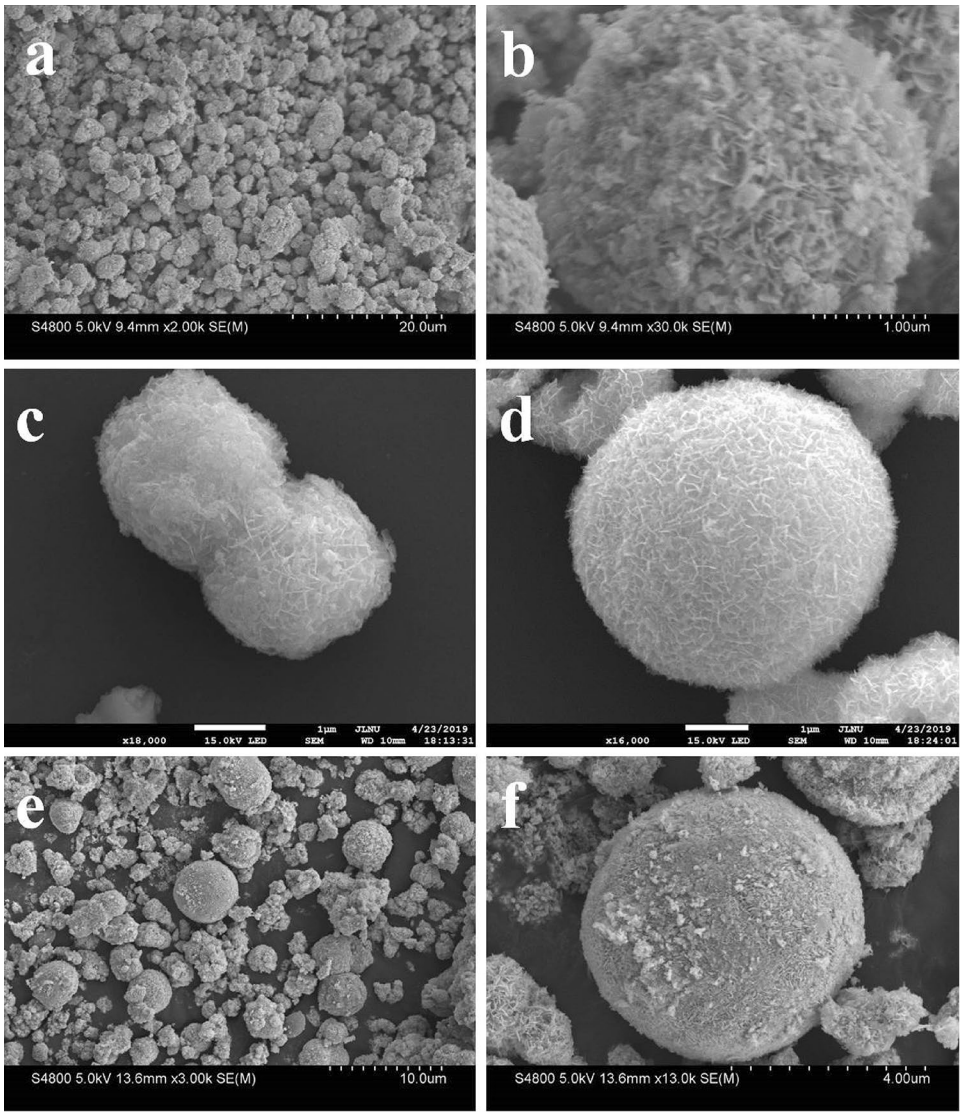

Fig. 4 **a**, **b** SEM images of BMO, **c**, **d** SEM images of SFO and **e**, **f** SEM images of 30 wt% SFO/BMO

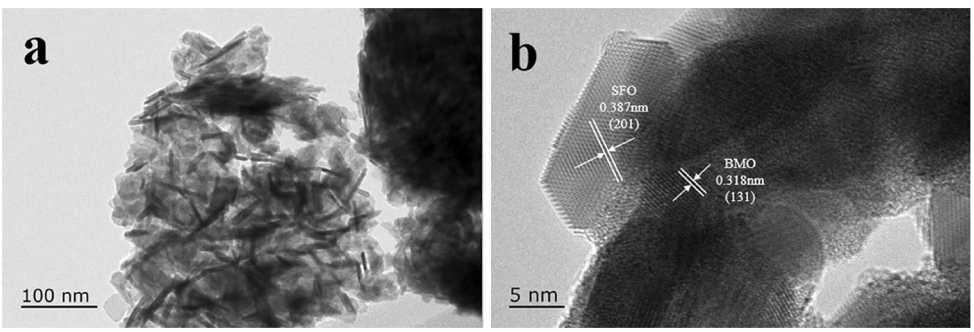

Fig. 5 **a** TEM image of 30 wt% SFO/BMO, **b** HRTEM image of 30 wt% SFO/BMO

indirect band gap semiconductor, so n = 4. As shown in Fig. 6b, c, the calculated forbidden band widths of BMO and SFO are 2.5 eV and 2.1 eV, respectively.

The position of the semiconductor's valence band (VB) and conduction band (CB) can be calculated according to the following formula:

$$E_{VB} = X - E^e + 0.5g \quad (3)$$

$$E_{VB} = X - E^e + 0.5g \quad (4)$$

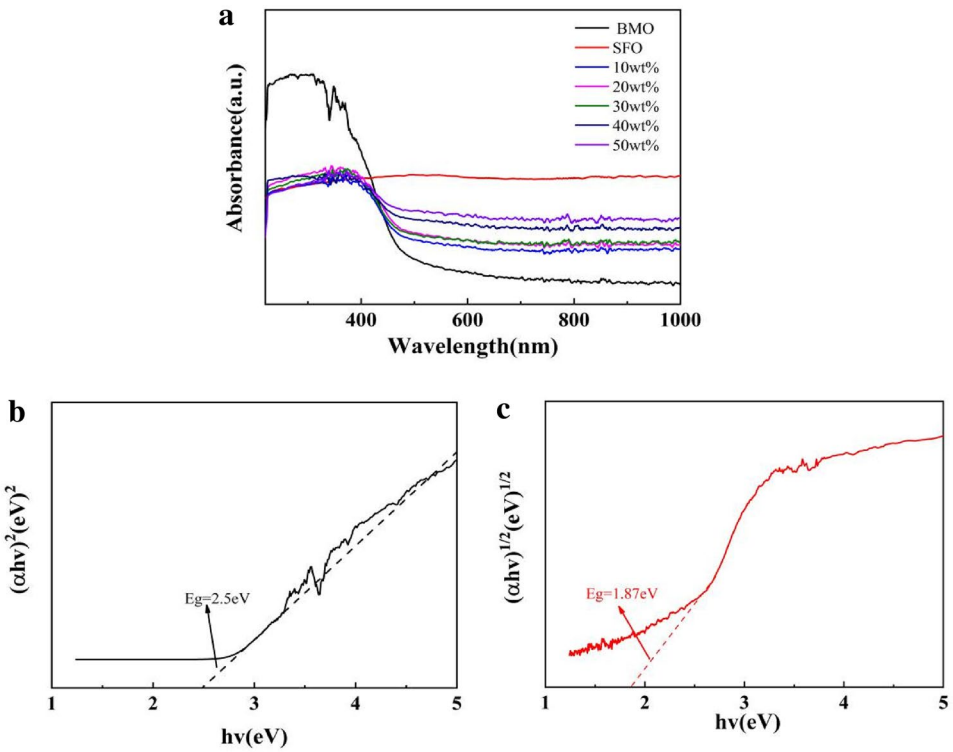

Fig. 6 **a** UV–Vis diffuse reflectance spectra of BMO, SFO and SFO/BMO, **b** the band gap spectrum of BMO and **c** band gap spectrum of SFO

where X refers to the electronegativity of the semiconductor, Ee is the energy of free electrons on the hydrogen scale, which is about 4.5 eV, and Eg is the band gap of the semiconductor [25, 41, 42]. Through calculation, the valence bands of BMO and SFO are 2.2 eV and 1.55 eV, respectively, while the conduction bands are − 0.3 eV and − 0.55 eV, respectively.

3.7 Photocatalytic Activity

The photocatalytic performance of the composite photocatalyst was evaluated by an experiment for degrading TC solution under simulated sunlight. 20 mg of different catalysts were added to a 30 mg/L TC solution, and a pure TC solution without any catalyst was used as a blank control. Firstly, a dark reaction period of 30 min was performed to make the photocatalyst and TC reach the adsorption equilibrium, and then the photoreaction phase of the xenon lamp irradiation was performed. It could be observed from Fig. 7a that within 100 min of photoreaction, the degradation efficiency of TC increased gradually with the increase of SFO content. When the content of SFO was 30 wt%, the degradation efficiency was 77% at the highest, which was 20.8% and 50.4% higher than 56.2% of BMO and 26.6% of SFO. This indicated that the formation of a heterojunction could improve the activity of the photocatalyst. However, as the mass ratio of SFO continued to increase, the degradation efficiency decreased gradually, which might be due to the weakening of the synergistic effect of the two materials by too much SFO.

The kinetic simulation of the photocatalytic degradation process of 30 wt% SFO/BMO heterojunction was carried out. The fitting results were shown in Fig. 7b, which showed that the TC degradation process of all catalysts follows a pseudo-first-order kinetics, $\ln(C_1/C) = kt$, where the slope k was the apparent first-order rate constant (min^{-1}) and C was the concentration at the irradiation time [43, 44]. According to calculations, the values of k were shown in Fig. 7c. It was clear that the first-order reaction kinetic constant k of 30 wt% SFO/BMO was the largest, indicating that the degradation rate was the fastest, and it was consistent with the conclusion of Fig. 7a. All of the above results indicated that the synergy between the reasonable composite ratios of SFO and BMO was beneficial to the improvement of the photocatalytic performance. In order to determine the stability of the heterojunction, the TC photocatalytic degradation experiment of 30 wt% SFO/BMO heterojunction was tested in a cycle. As shown in Fig. 7d, after five cycles of recovery tests, the degradation rate of TC decreased from 77 to 69.8%, indicating that the composite heterojunction had good stability in the photocatalytic reaction.

The raw and recycled materials were analyzed by X-ray photoelectron spectroscopy and X-ray diffraction. From Figs. 8 and 9, it could be seen that the properties of the recovered catalyst did not change. The stability of the catalyst had been further confirmed by the XPS and XRD.

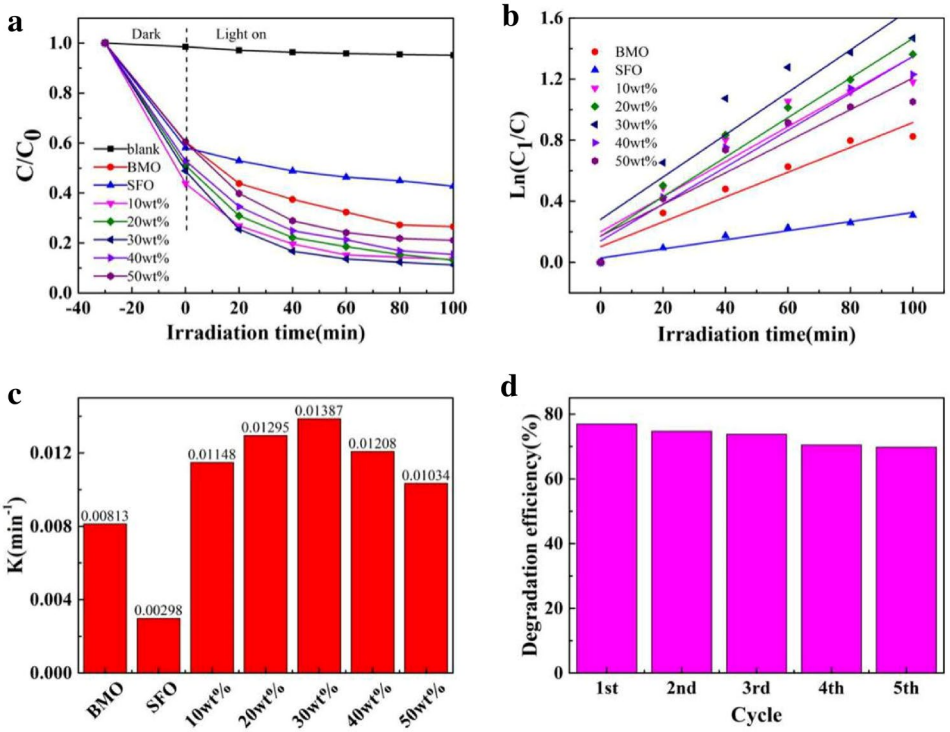

Fig. 7 **a** Photocatalytic activities of 30 wt% SFO/BMO for TC degradation, **b** the pseudo-first-order reaction kinetics curves for TC degradation, **c** the corresponding k values for TC degradation with different samples, and **d** TC degradation efficiency of 30 wt% SFO/BMO for 5 cycles of experiments

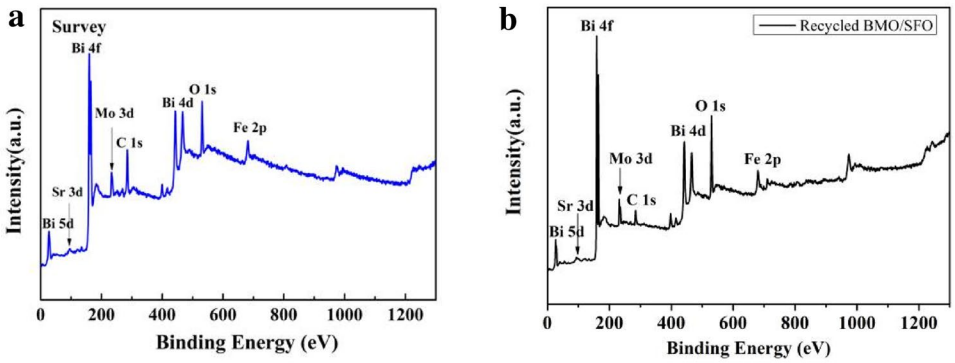

Fig. 8 **a** XPS spectrums of the raw materials and **b** recycled materials

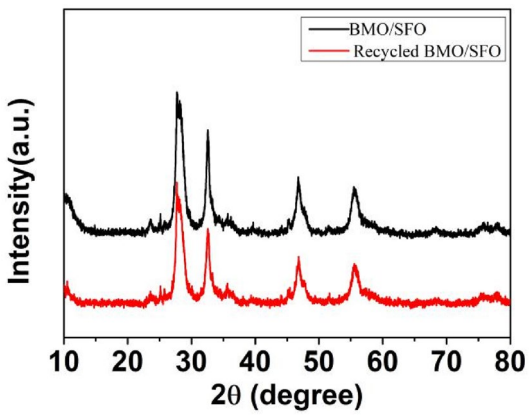

Fig. 9 XRD patterns of the raw materials and recycled materials

3.8 Photocatalytic Mechanism Analysis

Based on the above discussion, the photocatalytic mechanisms of the SFO/BMO heterostructures are proposed (Fig. 10). In the SFO/BMO heterostructure, the CB (− 0.55 eV) of SFO is more negative than that of BMO (− 0.3 eV), while the VB (2.2 eV) of BMO is more positive than that of SFO (1.55 eV), which shows an obvious type-II band alignment for SFO/BMO heterostructure. Moreover, the results are consistent with the reported references, such as $BiOI/Bi_2MoO_6$ [42], AgI/Bi_2MoO_6 [38], $AgI/CuBi_2O_4$ [39] and $NaNbO_3/Bi_2WO_6$ [45], indicating that the intimate hetero-interface and the formation of type-II heterogeneous structure are formed between BMO and SFO [46–48], which

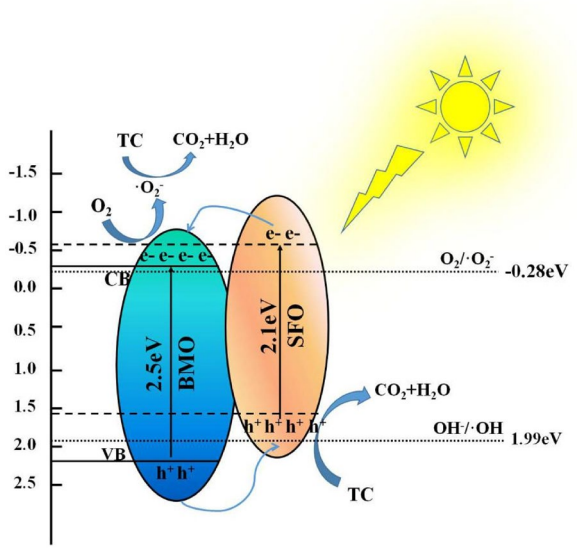

Fig. 10 Transfer of photogenerated carriers and mechanism diagram

effectively promotes the separation of electron–hole pairs and thus enhances the photocatalytic activity.

Figure 10 shows the entire process of the generation, transport and reaction of light carriers in the SFO/BMO heterojunction. With visible light irradiation, SFO and BMO can be triggered, produced electrons and holes on the conduction band and valence band respectively. Due to the more negative position of CB of SFO and the positive position of VB of BMO, at the interfaces between SFO and BMO, the photogenerated electrons on CB of SFO can transfer to the CB of the BMO, conversely, the holes on the VB of BMO can transfer to the VB of SFO, which makes the photogenerated electrons and holes effective separation. In addition, since the CB (− 0.3 eV) of BMO more negative than $O_2/\cdot O_2^-$ (− 0.28 eV), the electrons of CB of BMO are trapped by dissolved O_2 to generate a large amount of superoxide radicals with strong oxidizability, $\cdot O_2^-$. $\cdot O_2^-$ and h^+, which had strong oxidizing properties, will react with pollutants TC to produce CO_2 and H_2O without secondary pollution. The enhancement of the photocatalytic activity of the SFO/BMO heterojunction is attributed to type-II heterostructure systems formed between SFO and BMO, which effectively facilitates the separation of electron–hole pairs. The reactions that took place on the catalyst surface were as follows [49–56]:

$$\mathrm{SFO/BMO} + \mathrm{hv} \rightarrow \mathrm{SFO}\left(\mathrm{e}^- + \mathrm{h}^+\right)/\mathrm{BMO}\left(\mathrm{e}^- + \mathrm{h}^+\right) \quad (5)$$

$$\mathrm{SFO}\left(\mathrm{e}^- + \mathrm{h}^+\right)/\mathrm{BMO}\left(\mathrm{e}^- + \mathrm{h}^+\right) \rightarrow \mathrm{SFO}\left(\mathrm{h}^+\right) + \mathrm{BMO}\left(\mathrm{e}^-\right) \quad (6)$$

$$\mathrm{e}^- + \mathrm{O}_2 \rightarrow \cdot\mathrm{O}_2^- \quad (7)$$

$$\mathrm{h}^+ / \cdot \mathrm{O}_2^- + \mathrm{TC} \rightarrow \mathrm{CO}_2 + \mathrm{H}_2\mathrm{O} \quad (8)$$

4 Conclusions

The SFO/BMO heterojunction with different contents of SFO was synthesized by a simple hydrothermal method. Photocatalytic experiments showed that the prepared composite crystal exhibits enhanced degradation efficiency to TC compared to the original BMO and SFO. Meanwhile, when the mass ratio of SFO was 30 wt%, the SFO/BMO hydrothermal exhibited the highest photocatalytic activity and could degrade 77% of TC in 100 min. The improvement of photocatalytic activity was attributed to the proper band gap of the original material making it had good absorption of light and the large specific surface area increasing the reaction sites of the reactants and catalysts. And the most important reason was the formation of heterojunction. The recombination rate of electrons and holes was greatly reduced, thereby improving the photocatalytic performance. This work provided a reliable candidate for photocatalytic degradation of organic wastewater in the field of wastewater treatment and broadened the scope of application of modified BMO.

Acknowledgements This study was financially supported by the Fund Project of Shaanxi Key Laboratory of Land Consolidation (2019-JC03), Shaanxi Nature Science Basic Research Program (2019JM-429), Fundamental Research Funds for the Central Universities of Chang'an University (310829163406, 310829161002), Natural Science Foundation of China (21607015), Science & Technology Support Foundation of Shaanxi Province (2018JQ2025, 2016JQ2008). Chang'an University students' innovation program (S202010710130).

Compliance with Ethical Standards

Conflict of interest There are no conflict to declare.

References

1. Ni Z, Sun Y, Zhang Y, Fan D (2016) Fabrication, modification and application of $(BiO)_2CO_3$-based photocatalysts: a review. Appl Surf Sci 365:314–335. https://doi.org/10.1016/j.apsusc.2015.12.231
2. Guo J, Li P, Yang Z (2019) A novel Z-scheme g- C_3N_4/$LaCoO_3$ heterojunction with enhanced photocatalytic activity in degradation of tetracycline hydrochloride. Catal Commun 122:63–67. https://doi.org/10.1016/j.catcom.2019.01.022
3. Daghrir R, Drogui P (2013) Tetracycline antibiotics in the environment: a review. Environ Chem Lett 11(3):209–227. https://doi.org/10.1007/s10311-013-0404-8
4. Li J, Han M, Yang G et al (2016) Hydrothermal synthesis of novel flower-like $BiVO_4$/$Bi_2Ti_2O_7$ with superior photocatalytic activity

toward tetracycline removal. Appl Catal A Gen 524:105–114. https://doi.org/10.1016/j.apcata.2016.06.025
5. He R, Cao S, Peng Z, Yu J (2014) Recent advances in visible light Bi-based photocatalysts. Chinese J Catal 35(7):989–1007. https://doi.org/10.1016/S1872-2067(14)60075-9
6. Bai J, Li Y, Li X, Liu L (2017) Facile preparation of 2D Bi_2MoO_6 nanosheets-RGO composites with enhanced photocatalytic activity. New J Chem 41:7783–7790. https://doi.org/10.1039/c7nj01712j
7. Liang Q, Zhang M, Yao C et al (2017) High performance visible-light driven photocatalysts of Bi_2MoO_6–g–C_3N_4 with controllable solvothermal fabrication. J Photochem Photobiol A Chem 332:357–363. https://doi.org/10.1016/j.jphotochem.2016.09.012
8. Liu B, Liu X, Ni M et al (2018) SnO_2 as co-catalyst for enhanced visible light photocatalytic activity of Bi_2MoO_6. Appl Surf Sci 453:280–287. https://doi.org/10.1016/j.apsusc.2018.05.040
9. Liang J, Liu F, Deng J et al (2017) Efficient bacterial inactivation with Z-scheme AgI/Bi_2MoO_6 under visible light irradiation. Water Res 123:632–641. https://doi.org/10.1016/j.watres.2017.06.060
10. Ke J, Duan X, Luo S et al (2017) UV-assisted construction of 3D hierarchical rGO/Bi_2MoO_6 composites for enhanced photocatalytic water oxidation. Chem Eng J 313:1447–1453. https://doi.org/10.1016/j.cej.2016.11.048
11. Dai Z, Fan Q, Zhao H et al (2016) crystal defect engineering of aurivillius Bi_2MoO_6 by Ce doping for increased reactive species production in photocatalysis. ACS Catal 6(5):3180–3192. https://doi.org/10.1021/acscatal.6b00490
12. Zhen H, Khan MA, Xia M et al (2019) Controllable synthesis of flower-root shaped Bi_2O_3/Bi_2MoO_6 heterostructures as an efficient photocatalyst under visible light irradiation. J Photochem Photobiol A Chem 372:78–88. https://doi.org/10.1016/j.jphotochem.2018.11.021
13. Xu YS, Zhang ZJ, Zhang WD (2013) Facile preparation of heterostructured Bi_2O_3/Bi_2MoO_6 hollow microspheres with enhanced visible-light-driven photocatalytic and antimicrobial activity. Mater Res Bull 48(4):1420–1427. https://doi.org/10.1016/j.materresbull.2012.12.063
14. Tao R, Shao C, Li X et al (2018) $Bi_2MoO_6/BiFeO_3$ heterojunction nanofibers: enhanced photocatalytic activity, charge separation mechanism and magnetic separability. J Colloid Interface Sci 529:402–414. https://doi.org/10.1016/j.jcis.2018.06.035
15. Wan R, Jia C, Zhang W (2012) Preparation and photoelectric properties of p-$CaFe_2O_4$/n–WO_3 composites. J Alloys Compd 544:1–5. https://doi.org/10.1016/j.jallcom.2012.07.134
16. Shifu C, Wei Z, Wei L et al (2009) Preparation, characterization and activity evaluation of p–n junction photocatalyst p-$CaFe_2O_4$/n–ZnO. Chem Eng J 155:466–473. https://doi.org/10.1016/j.cej.2009.07.009
17. Nadeem ZM, Mufarah A, Mehwish T et al (2018) $SrFe_2O_4$ nanoferrites and $SrFe_2O_4$/ground eggshell nanocomposites: fast and efficient adsorbents for dyes removal. J Clean Prod 199:983–994. https://doi.org/10.1016/j.jclepro.2018.07.204
18. Majid A, Tunney J, Argue S et al (2005) Preparation of $SrFeO_{\sim 2.85}$ perovskite using a citric acid assisted Pechini-type method. J Alloy Compd 398:48–54. https://doi.org/10.1016/j.jallcom.2005.02.023
19. Ghaffari M, Pei YT, Oruc ME et al (2011) Effect of ball milling on the characteristics of nano structure $SrFeO_3$ powder for photocatalytic degradation of methylene blue under visible light irradiation and its reaction kinetics. Catal Today 161(1):70–77. https://doi.org/10.1016/j.cattod.2010.11.031
20. Xie T, Xu L, Liu C, Wang Y (2013) Magnetic composite $ZnFe_2O_4$/$SrFe_{12}O_{19}$: preparation, characterization, and photocatalytic activity under visible light. Appl Surf Sci 273:684–691. https://doi.org/10.1016/j.apsusc.2013.02.113
21. Vijayaraghavan T, Suriyaraj SP, Selvakumar R et al (2016) Rapid and efficient visible light photocatalytic dye degradation using AFe_2O_4 (A=Ba, Ca and Sr) complex oxides. Mater Sci Eng B. https://doi.org/10.1016/j.mseb.2016.04.005
22. Dumrongrojthanath P, Phuruangrat A, Thongtem S, Thongtem T (2019) Hydrothermal synthesis and characterization of visible light-driven I-doped Bi_2MoO_6 photocatalyst. J Iran Chem Soc 16:733–739. https://doi.org/10.1007/s13738-018-1550-5
23. Wu J, Sun Y, Gu C et al (2018) Pt supported and carbon coated Bi_2MoO_6 composite for enhanced 2,4–dibromophenol degradation under visible–light irradiation: insight into band gap structure and photocatalytic mechanism. Appl Catal B Environ 237:622–632. https://doi.org/10.1016/j.apcatb.2018.06.016
24. Wang J, Sun Y, Wang Z et al (2019) Synthesis and enhanced photocatalytic activity of visible-light-driven co-doped Bi_2MoO_6 photocatalyst with flower-like nanostructures. Russ J Phys Chem A 93:736–742. https://doi.org/10.1134/S0036024419040307
25. Zhang Z, Zheng T, Xu J et al (2017) Carbon quantum dots/Bi_2MoO_6 composites with photocatalytic H_2 evolution and near infrared activity. J Photochem Photobiol A Chem 346:24–31. https://doi.org/10.1016/j.jphotochem.2017.05.029
26. Bo L, Hu Y, Zhang Z, Tong J (2019) Efficient photocatalytic degradation of Rhodamine B catalyzed by $SrFe_2O_4$/g-C_3N_4 composite under visible light. Polyhedron 168:94–100. https://doi.org/10.1016/j.poly.2019.04.036
27. Xu YS, Zhang WD (2013) Monodispersed Ag_3PO_4 nanocrystals loaded on the surface of spherical Bi_2MoO_6 with enhanced photocatalytic performance. Dalt Trans 42:1094–1101
28. Chen Y, Tian G, Shi Y et al (2015) Hierarchical MoS_2/Bi_2MoO_6 composites with synergistic effect for enhanced visible photocatalytic activity. Appl Catal B Environ 164:40–47
29. Anukorn P, Thitirat K, Panudda P et al (2020) Synthesis of Pd nanoparticles modified Bi_2MoO_6 nanoplates by microwave-assisted deposition with their enhanced visible-light-driven photocatalyst. Optik 212:164474. https://doi.org/10.1016/j.ijleo.2020.164674
30. Shi W, Li M, Huang X et al (2020) Construction of $CuBi_2O_4$/Bi_2MoO_6 p–n heterojunction with nanosheets-on-microrods structure for improved photocatalytic activity towards broad-spectrum antibiotics degradation. Chem Eng J 394(2020):125009–125018. https://doi.org/10.1016/j.cej.2020.125009
31. Ranjana V, Shivkumar C, Nainesh P et al (2020) Interplay of adsorption, photo-absorption, electronic structure and charge carrier dynamics on visible light driven photocatalytic activity of Bi_2MoO_6/rGO (0D/2D) heterojunction. J Environ Chem Eng. https://doi.org/10.1016/j.jece.2020.1045
32. Yin L, Guo E (2015) Tailored $SrTiO_3/TiO_2$ heterostructures for dye-sensitized solar cells with enhanced photoelectric conversion performance. J Mater Chem A 3(25):13390–13401
33. Lee SW, Kim S, Bae S et al (2018) Enhanced UV stability of perovskite solar cells with a SrO interlayer. Org Electron 63:343–348
34. Ghaffari M, Huang H, Tan OK, Shannon M (2012) Band gap measurement of $SrFeO_3$−δ by ultraviolet photoelectron spectroscopy and photovoltage method. CrystEngComm 14:7487–7749
35. Guo JF, Yang CS, Sun ZX et al (2020) Ternary Fe_3O_4/MoS_2/$BiVO_4$ nanocomposites: novel magnetically separable visible-light-driven photocatalyst for efficiently degradation of antibiotic wastewater through p-n heterojunction. J Mater Sci-Mater Electron 31:16746–16758. https://doi.org/10.1007/s10854-020-04230-9
36. Suqin L, Li W, Gaopeng D, Qiufei H (2017) Fabrication of $Ag_2CO_3/SrCO_3$ rods with highly efficient visible-light photocatalytic activity. Rare Met Mater Eng 46:312–316. https://doi.org/10.1016/s1875-5372(17)30086-3
37. Wang Z, Wang K, Li Y et al (2019) Novel BiSbO4/BiOBr nanoarchitecture with enhanced visible-light driven photocatalytic performance: oxygen-induced pathway of activation and mechanism

unveiling. Appl Surf Sci 498:14385. https://doi.org/10.1016/j.apsusc.2019.143850
38. Tian G, Chen Y, Zhou W et al (2010) Facile solvor thermal synthesis of hierarchical flower-like Bi_2MoO_6 hollow spheres as high peformance visible-light driven photocatalysts. J Mater Chem 21(3):887–892. https://doi.org/10.1039/C0JM03040F
39. Wang K, Li J, Zhang G (2019) Ag-bridged Z-scheme 2D/2D Bi_5FeTi_3O15/g-C_3N_4 heterojunction for enhanced photocatalysis: mediator-induced interfacial charge transfer and mechanism insights. ACS Appl Mater Interfaces 11(31):27686–27696. https://doi.org/10.1021/acsami.9b05074
40. Jiang TG, Wang K, Guo T et al (2020) Fabrication of Z-scheme MoO_3/Bi_2O_4 heterojunction photocatalyst with enhanced photocatalytic performance under visible light irradiation. Chin J Catal 41(1):161–169. https://doi.org/10.1016/S1872-2067(19)63391-7
41. Zhang M, Shao C, Mu J et al (2011) One-dimensional Bi_2MoO_6/TiO_2 hierarchical heterostructures with enhanced photocatalytic activity. CrystEngComm 14:605–612. https://doi.org/10.1039/c1ce05974b
42. Zhou G, Tian Z, Sun H et al (2020) Understanding the photocatalytic mechanisms of the $BiOI/Bi_2MoO_6$ and $BiOCl/Bi_2MoO_6$ heterostructures: first-principles study. J Phys Chem Solids 146:109577. https://doi.org/10.1016/j.jpcs.2020.109577
43. Xu M, Zhang W (2016) Facile preparation of AgI/Bi_2MoO_6 heterostructured photocatalysts with enhanced photocatalytic activity. EUR J Inorg Chem. https://doi.org/10.1002/ejic.201501260
44. Guo F, Shi W, Wang H et al (2018) Study on highly enhanced photocatalytic tetracycline degradation of type II $AgI/CuBi_2O_4$ and Z-scheme $AgBr/CuBi_2O_4$ heterojunction photocatalysts. J Hazard Mater 349:111–118. https://doi.org/10.1016/j.jhazmat.2018.01.042
45. Qiao Y, Meng X, Zhang Z (2018) A new insight into the enhanced visible light-induced photocatalytic activity of $NaNbO_3/Bi_2WO_6$ type-II heterostructure photocatalysts. Appl Surf Sci 470:645–657. https://doi.org/10.1016/j.apsusc.2018.11.048
46. Kar A, Sain S, Rossouw D et al (2017) Targeting low-cost type-II heterostructures: synthesis, structure and photoreactivity. J Alloy Compd 698:944–956. https://doi.org/10.1016/j.jallcom.2016.12.167
47. Zeng W, Cao S, Qiao L et al (2019) One-pot nitridation route synthesis of $SrTaO_2N/Ta_3N_5$ type II heterostructure with enhanced visible-light photocatalytic activity. J Colloid Interface Sci 554:74–79. https://doi.org/10.1016/j.jcis.2019.06.097
48. Selvaraj R, Kalimuthu KR, Kalimuthu V (2019) A type-II MoS_2/ZnO heterostructure with enhanced photocatalytic activity. Mater Lett 243:183–186. https://doi.org/10.1016/j.matlet.2019.02.022
49. Tian Y, Cheng F, Zhang X et al (2014) Solvothermal synthesis and enhanced visible light photocatalytic activity of novel graphitic carbon nitride-Bi_2MoO_6 heterojunctions. Powder Technol 267:126–133. https://doi.org/10.1016/j.powtec.2014.07.021
50. Feng G, Shi W, Wang H et al (2017) Facile fabrication of CoO/g–C3N4 p–n heterojunction with enhanced photocatalytic activity and stability for tetracycline degradation under visible light. Catal Sci Technol 7(15):3325–3333. https://doi.org/10.1039/c7cy00960g
51. Marschall R (2014) Semiconductor composites: strategies for enhancing charge carrier separation to improve photocatalytic activity. Adv Funct Mater 24:2420. https://doi.org/10.1002/adfm.201470108
52. Li Z, Meng X, Zhang Z (2018) Few-layer MoS_2 nanosheets-deposited on Bi_2MoO_6 microspheres: a Z-scheme visible-light photocatalyst with enhanced activity. Catal Today 315:67–78. https://doi.org/10.1016/j.cattod.2018.03.014
53. Yin Z, Tian YJ, Gao P et al (2020) Photodegradation mechanism and genetic toxicity of bezafibrate by Pd/g–C3N4 catalysts under simulated solar light irradiation: the role of active species. Chem Eng J 379:122294–122304. https://doi.org/10.1016/j.cej.2019.122294
54. Zhang H, Jia Q, Lai L et al (2019) Degradation of p-nitrophenol (PNP) in aqueous solution by mFe/Cu-airPS system. Chin Chem Lett 30:1129–1132. https://doi.org/10.1016/j.cclet.2019.01.025
55. Yin Z, Han MG, Hu Z et al (2020) Peroxymonosulfate enhancing visible light photocatalytic degradation of bezafibrate by Pd/g–C_3N_4 catalysts: the role of sulfate radicals and hydroxylradicals. Chem Eng J 390(2020):124532–124542. https://doi.org/10.1016/j.cej.2020.124532
56. Li J, Li Y, Xiong Z et al (2019) The electrochemical advanced oxidation processes coupling of oxidants for organic pollutants degradation: a mini-review. Chin Chem Lett 30:2139–2146. https://doi.org/10.1016/j.cclet.2019.04.057

Affiliations

Jifeng Guo[1,2] · Rui Liu[1,2] · Yuxuan Ma[1,2] · Meiqi Wang[1,2] · Jing Li[1,2] · Xiao Wei[1,2] · Luyao Zhao[1,2]

[1] Key Laboratory of Subsurface Hydrology and Ecological Effects in Arid Region, Ministry of Education, Chang'an University, Xi'an 710054, People's Republic of China

[2] School of Water and Environment, Chang'an University, Xi'an 710054, People's Republic of China